Research Article | Vol. 9, No. 11 | 1 Nov 2018 | BIOMEDICAL OPTICS EXPRESS 5400
Biomedical Optics EXPRESS

Characterization of human cutaneous tissue autofluorescence: implications in topical drug delivery studies with fluorescence microscopy

MAIKO HERMSMEIER,[1,*] SINYOUNG JEONG,[2] AKIRA YAMAMOTO,[1] XIN CHEN,[1] USHA NAGAVARAPU,[1] CONOR L. EVANS,[2] AND KIN F. CHAN[1]

[1]*BioPharmX, Inc., 1505 Adams Drive Suite D, Menlo Park, CA 94025, USA*
[2]*Wellman Center for Photomedicine, Massachusetts General Hospital and Harvard Medical School, Boston, MA 02114, USA*
[*]*mhermsmeier@gmail.com*

Abstract: In pharmacokinetic studies of topical drugs, fluorescence microscopy methods can enable the direct visualization and quantification of fluorescent drugs within the skin. One potential limitation of this approach, however, is the strong endogenous fluorescence of skin tissues that makes straightforward identification of specific drug molecules challenging. To study this effect and quantify endogenous skin fluorescence in the context of topical pharmacokinetics, an integrating sphere-based screening tool was designed to collect fluorescence yield data from human skin specimens. Such information could be utilized to select specific donors in the investigation of drug uptake and distribution. Results indicated human facial skin specimens from a group of more than 35 individuals exhibited an at least 6-fold difference in endogenous fluorescence. In visualizing drug distributions, the negative impact of autofluorescence could be exacerbated in cases where there are overlapping spatial distributions or spectral emission profiles between endogenous fluorophores and the exogenous fluorophore of interest. We demonstrated the feasibility of this approach in measuring the range of tissue endogenous fluorescence and selecting specimens for the study of drug pharmacokinetics with fluorescence microscopy.

1. Introduction

Radiolabeling has been the mainstay for assessing drug distribution within tissue or organs in the pharmaceutical industry, using both quantitative whole-body autoradiography (QWBA) [1–3] and microautoradiography (MARG) [4] tools. However, QWBA is limited in resolving power when submillimeter resolution is required [3], and radiolabeling can potentially change the pharmacokinetics of the drug. Recent advances in mass spectrometry [1–3], matrix assisted laser desorption/ionization (MALDI) [3], and variants [5] of mass spectrometric imaging (MSI) have provided two-dimensional mapping of drug distribution with high specificity and resolution without the need to modify the target drug. Unfortunately, MSI is a destructive technique not amenable to *in vivo* clinical studies, and is time consuming and economically formidable when conducting large and repeated studies.

The potential of nonlinear optical microscopy has recently been explored for the visualization of drug distributions [6–9]. Thorling et al. [7] showed the distribution of fluorescein and its metabolites in an *in vivo* rat model using multiphoton microscopy and fluorescent lifetime imaging (FLIM). El-Mashtoly et al. [8] demonstrated the use of Raman microscopy in tracking the cellular distribution of label-free erlotinib, a tyrosine kinase inhibitor targeting the epidermal growth factor receptor (EGFR) for cancer treatment [9].

We have recently demonstrated the visualization of minocycline hydrochloride, an antibiotic used in the treatment of acne vulgaris, in excised human facial skin specimens using conventional fluorescence microscopy with concurrent high-performance liquid

#341314 https://doi.org/10.1364/BOE.9.005400
Journal © 2018 Received 6 Aug 2018; revised 27 Sep 2018; accepted 5 Oct 2018; published 12 Oct 2018

Biomedical Optics EXPRESS

chromatography (HPLC) quantification to assess the total drug penetration for a topical minocycline gel [10]. Though the signal-to-noise ratio of conventional fluorescence microscopy limited its usage to high doses (e.g. a so-called 'infinite' dose) of drug application, a trend in fluorescence intensity and distribution was perceptible at different concentration levels. Additionally, by using two-photon fluorescence lifetime imaging microscopy (TP-FLIM) with non-Euclidean phasor analysis, the selective visualization of minocycline fluorescence in the target pilosebaceous unit at lower dosages of about 2.5 × daily dose was achieved [11]. However, it was still noted that the level of autofluorescence in the specimens significantly affected the detectability of the drug's fluorescence signal as the spectral overlap of the two presented significant challenges to straightforward spectral discrimination.

The causative changes and differences in the level of human skin autofluorescence are believed to be multi-factorial [12]. Aging [13] and the skin microbiome [14] are potential reasons for changes in skin autofluorescence. Lifestyle [15–17] such as diet, cosmetic use, and regular flavonoid intake appeared to have quantifiable effects in epidermal and dermal endogenous fluorescence. Pre-existing health conditions [18–21] such as type II diabetes, cardiovascular, Alzheimer's or other degenerative diseases that result in the accumulation of advanced glycation end-product produce photosensitizing agents in the skin that could affect its endogenous fluorescence. Additionally, certain active pharmaceutical ingredients [22,23] such as antibiotics, retinoids, and photodynamic drugs could affect the skin baseline fluorescence.

As these factors can present substantial confounding variables in studying the pharmacokinetics of naturally fluorescent drug compounds, one promising approach would be to use endogenous skin autofluorescence levels as a pre-screening step. We hypothesize that selecting tissue from study subjects with low endogenous fluorescence could lead to an improvement in the sensitivity of fluorescence drug detection techniques. If this hypothesis is correct, the design of clinical trials could include a sub-population of subjects with low endogenous fluorescence that could enable *in vivo* imaging study of drug pharmacokinetics – Pharmacokinetic Tomography. In this article, we explore the use of an integrating sphere in screening autofluorescence in human facial skin specimens for potential prior selection and conduct of topical drug delivery studies.

2. Materials and methods

2.1 Experimental materials

Excised human periauricular facial skin from facelift patients were obtained and stored at −80 °C. Prior to experimentation, a portion of the specimen was removed and thawed. The tissues were OCT-embedded and frozen-sectioned cross-sectionally along the plane perpendicular to the skin surface using a cryostat (Leica CM1850 UV, Buffalo Grove, IL). A 50-µm thick section was mounted on a microscope slide (Thermo Scientific Superfrost Plus, Waltham, MA) for the integrating sphere method. A 30 µm thick section from the same tissue block was mounted on microscope slide (Fisherbland ColorFrost microscope slide, Thermo Fisher Scientific, Hampton, NH) for Two-Photon Excited Fluorescence (TPEF) microcopy.

2.2 Autofluorescence screening

2.2.1 Experimental setup: integrating sphere and conventional fluorescence microscopy

An inverted fluorescence microscope (Zeiss Axiovert 100M, Pleasanton, CA) was used with an excitation-emission filter pair. A 40X objective lens with 0.65NA, an excitation bandpass filter with a center wavelength of 386 nm ($\Delta\lambda$ = 27 nm @ FWHM; ≥ OD6.0), a dichroic beamsplitter with a passband of 450-680 nm @ FWHM (50% transmittance) and a dual-band emission filter (450-480 nm and 610-680 nm @ FWHM) were used, as shown in Fig. 1.

Biomedical Optics EXPRESS

For fluorescence screening, photocurrent measurements were performed with a Si photodetector (Thorlabs SM05PD1B, Newton, NJ) mounted to the output port of an integrating sphere (Thorlabs IS236A-4, Newton, NJ), and connected to a photodiode amplifier (Thorlabs PDA200C, calibrated, Newton, NJ). The amplifier chassis was electrically grounded to minimize electromagnetic interference and an oscilloscope was used to monitor signal fluctuation. The integrating sphere consisted of a 2-inch diameter internal cavity and was placed above the slide mount on the fluorescence microscope as illustrated in Fig. 1. A longpass filter with a cut-on wavelength at 450 nm (≥ OD4.0 below cut-on) was attached to an open port, orthogonal to the position of the output/detector port. The open port aperture is centered along the optical axis of the microscope objective lens. This setup ensured that integrating sphere collected fluorescence emission above 450 nm while minimizing any residual excitation light. Because the excitation source on the microscope is not close-loop controlled, a warm-up period of at least one hour was allowed to ensure the source was stabilized prior to each experimental session. The optical power from the excitation source was then measured. Measurements were made with Intralipid-10% [24] as the scattering reference standard to monitor excitation source stability. As such, a demountable cuvette (FireflySci Type 19 cell, Staten Island, NY) with a 50-μm lightpath filled with Intralipid-10% (75849-312, VWR, Radnor, PA; 20% intralipid was diluted to 10% with deionized water) was used. Inset in Fig. 1 indicates photocurrent measurements with Intralipid-10% was stable within 10% range over a period of 7 days.

The sample was placed on the slide mount, with the microscope slide inverted such that the tissue was facing the objective lens. An initial photocurrent measurement was made through the blank portion of the microscope slide as the baseline. Photocurrent resulting from tissue fluorescence was recorded and fluorescence images of the tissue specimens originating from the same field of view (FOV) of the corresponding photocurrent measurements were captured.

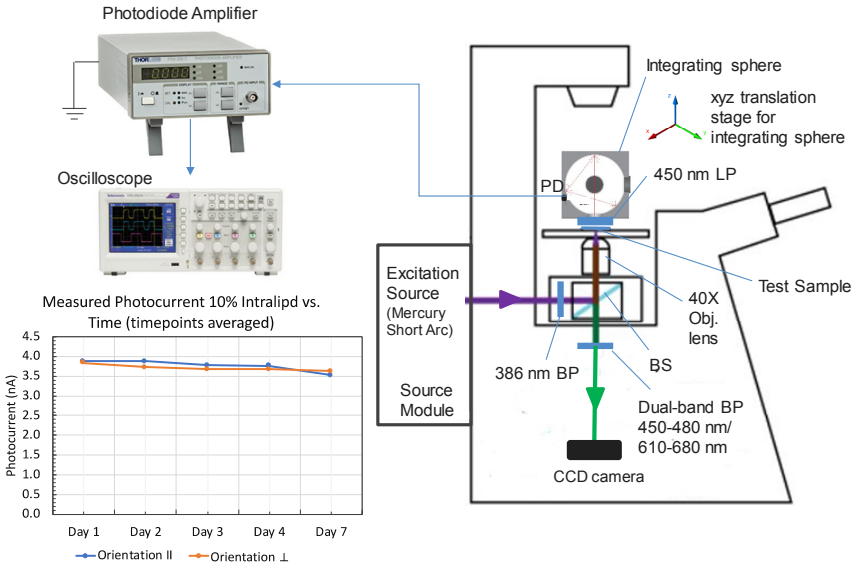

Fig. 1. Fluorescence emission screening experimental setup. Concurrent image capture of tissue section within the same FOV (same as 386-nm excitation cross-section) was performed with conventional fluorescence microscopy. Lower left inset indicates Intralipid-10% photocurrent measurements for a 7-day period to monitor excitation source stability. PD: Photodetector; BP: Bandpass filter; LP: Longpass filter; BS: Dichroic Beamsplitter; xyz translation stage not shown diagrammatically; 40 × objective lens, 0.65NA.

Biomedical Optics EXPRESS

2.2.2 Total fluorescence and fluorescence yield approximation

2.2.2.1 Theory of operation

Figure 2 shows the radiant power of autofluorescence generated by tissue, Φ_s, the resulting radiant power collected by the integrating sphere, Φ_i, and the radiant power as measured by the photodetector, Φ_d.

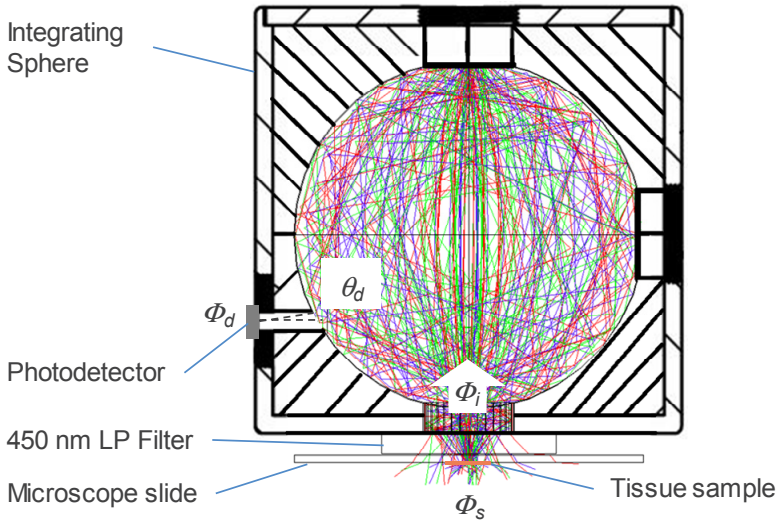

Fig. 2. Geometry of autofluorescence collection with an integrating sphere from tissue sample. Dimension of tissue sample in this figure is exaggerated for illustration purpose only, while the remainder of the drawing is to-scale. The ray-tracing in this figure is for illustration purpose only. The integrating sphere transfer function (Φ_i /Φ_d) value was analytically estimated to be 947 using Eq. (4), and confirmed with a measured value of 969 using a 532-nm diffused source, as indicated in Fig. 4 below.

The radiant power measured by the photodetector, Φ_d, can be expressed as [25]

$$\Phi_d = L_{sph} A_d \Omega \tag{1}$$

where L_{sph} is the integrating sphere surface radiance (W/cm^2.sr), A_d is the detector area within the projected solid angle, Ω, where $\Omega = \pi.sin^2\theta_d$, with θ_d as the photodetector acceptance angle. Φ_d is expressed in units of Watts. Converted from measured photocurrent, i_d, in units of Amperes (Amps), and assuming known wavelength-dependent responsivity, $\Re$, in Amps/Watt of the photodetector, Φ_d can also be expressed with the relation

$$\Re(\lambda) = \frac{i_d}{d} \tag{2}$$

As a result of the radiant power collected by the integrating sphere, Φ_i, the surface radiance L_{sph} may be expressed as [25]

$$L_{sph} = \frac{\Phi_i}{\pi.A_s} \frac{\rho}{\left[1-\rho(1-f)\right]} = \frac{\Phi_i}{\pi.A_s} M \tag{3}$$

where A_s is the internal surface area of the integrating sphere, ρ is the reflectance, f is the port fraction; $f = (A_i + A_d)/A_s$, where A_i is the area of the input port, and A_d is the area of the output/detector port. The term $\frac{\rho}{\left[1-\rho(1-f)\right]}$ is a dimensionless sphere multiplier, M.

Biomedical Optics EXPRESS

From Eqs. (1) and (3), the integrating sphere transfer function, Φ_i/Φ_d, is then

$$\frac{\Phi_i}{\Phi_d} = \frac{A_s}{A_d} \cdot \frac{1}{M.\sin^2\theta_d} \tag{4}$$

Φ_i may be approximated from the total fluorescence radiant power, Φ_s, originating from the tissue section by

$$\Phi_i = \frac{\Phi_s}{2} \cdot \frac{r'^2 \int_0^{2\pi} d\phi \int_0^{\theta_i} \sin\theta d\theta}{r'^2 \int_0^{2\pi} d\phi \int_0^{\pi} \sin\theta d\theta} = \frac{\Phi_s}{2} \cdot \gamma \tag{5}$$

where $\Phi_s = 2\pi^2 r^2 L_s$. Assuming autofluorescence emission from the illuminated tissue cross-section is a Lambertian disk source, L_s is therefore a constant radiance emitted from an area within a radius r of the tissue section [25,26] for a thin disk (r >> section thickness). A factor of two in Eq. (5) indicates only half of the fluorescence emission from the top surface of the tissue cross-section was considered. Fluorescence emission among endogenous fluorophores is assumed isotropic. Hence, whatever fluorescence was captured by the integrating sphere there was an equal amount lost to the opposite direction, requiring a factor of 2 correction. The ratio $\gamma = \frac{r'^2 \int_0^{2\pi} d\phi \int_0^{\theta_i} \sin\theta d\theta}{r'^2 \int_0^{2\pi} d\phi \int_0^{\pi} \sin\theta d\theta}$ denotes the autofluorescence fraction collected within the integrating sphere's acceptance angle θ_i, located approximately at a distance r', from the UV-illuminated segment of the tissue (Fig. 3). Based on the geometry of this setup, the acceptance angle, θ_i, is approximately 45.7 deg (Table 1), corresponding to an NA ~0.72. A spherical wavefront approximation was used here for autofluorescence fraction with the assumption that the aperture radius, $D_i/2 >> r$, the source radius (Fig. 3).

From Eqs. (4) and (5), the total fluorescence transfer function, Φ_s/Φ_d, is then

$$\frac{\Phi_s}{\Phi_d} = \frac{2A_s}{\gamma A_d} \cdot \frac{1}{M.\sin^2\theta_d} \tag{6}$$

Table 1 lists the physical input parameters of the integrating sphere setup for fluorescence yield measurements. The integrating sphere transfer function (Φ_i/Φ_d) value was calculated to be 947. Subsequent calibration of the integrating sphere with a diffused 532-nm laser source produced a corresponding Φ_i/Φ_d transfer function value of 969 (Fig. 4) with an R^2 of 0.9995 by linear regression (r = 0.9997, p < 0.001 by Pearson's Correlation), in close agreement with the theoretical estimate.

Based on the experimental design geometry, the integrating sphere input port acceptance angle, θ_i, was estimated to be about 45.7 deg (Fig. 3 and Table 1), resulting in a fluorescence collection fraction, γ, of 0.15, and a total fluorescence transfer function, Φ_s/Φ_d, of 12635. From the photodetector measurements of the incident radiant power, Φ_d, the total fluorescence radiant power, Φ_s, may be approximated as follows:

$$\Phi_s = 12635\Phi_d \qquad \text{Eq. (7)}$$

Biomedical Optics EXPRESS

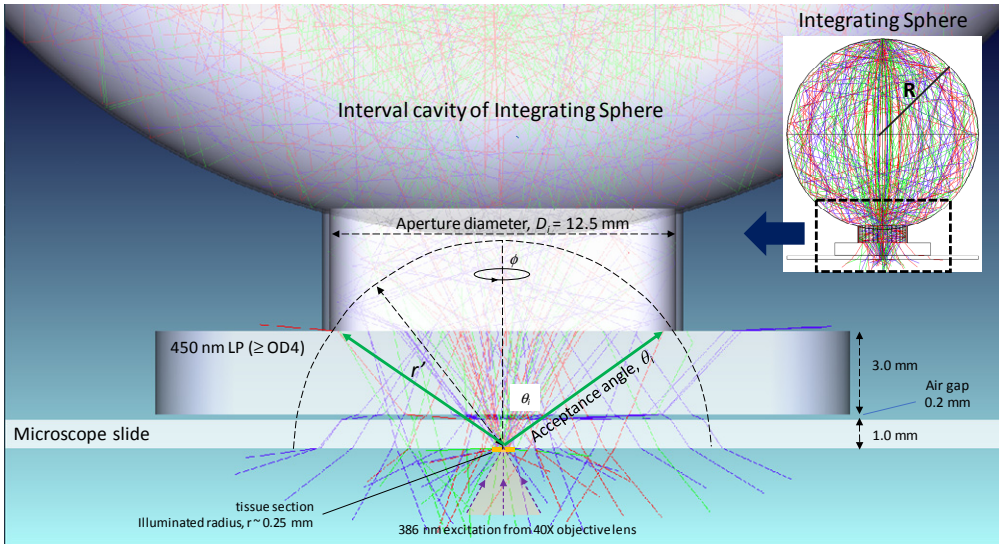

Fig. 3. Total fluorescence emission detection geometry. Fluorescence was collected within the angular acceptance as shown at wavelengths above 450 nm (≥ OD4.0 below cut-on). Excitation wavelength is centered at 386 nm with a passband of 27 nm at FWHM (≥ OD6.0 above cut-off) delivered with a 40 × objective lens, 0.65NA. LP: 450-nm longpass filter.

Table 1. Physical parameters of fluorescence measurement setup. Theoretical estimate based on values in the table below produced an integrating sphere transfer function (Φ_i /Φ_d) value of 947.

INPUT PARAMETERS	VALUES
Output/Detector Port Area (cm^2), A_d	0.0707
Photodetector Acceptance Angle (deg), θ_d	10.24
Detector Acceptance Angle, Ω	0.099
Detector Responsivity (A/W) @ 532 nm, $\Re$	0.33
Detector Responsivity (A/W) @ 550 nm, $\Re$	0.35
Integrating Sphere Reflectance, ρ	0.99
Input Port Area (cm^2), A_i	1.23
Integrating Sphere Surface Area (cm^2), A_s	81.07
Sphere Multiplier, M	38.3
Integrating Sphere Acceptance Angle (deg), θ_i	45.7

Biomedical Optics EXPRESS

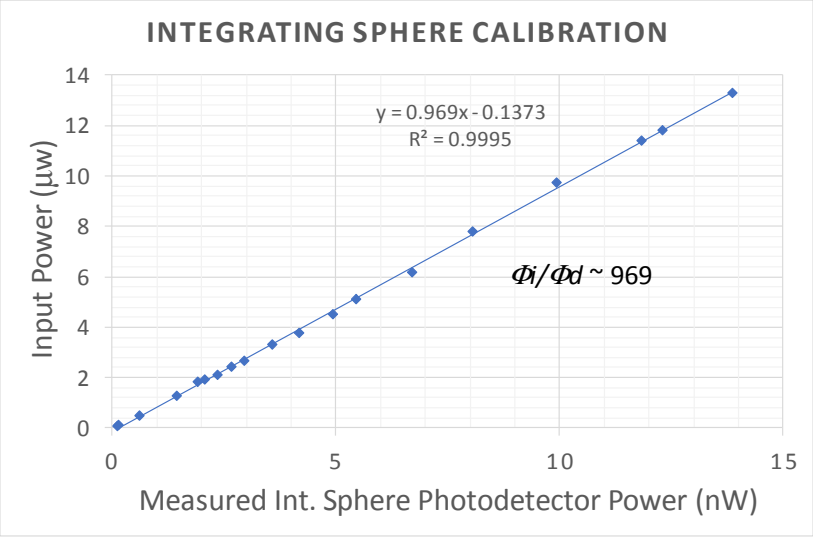

Fig. 4. Calibration of integrating sphere with a 532-nm diffused source an integrating sphere transfer function (Φ_i /Φ_d) value of 969.

2.2.2.2 Total fluorescence and fluorescence radiance emission

For each tissue sample, the photocurrents and images were recorded at locations in the epidermis, hair follicle, or sebaceous gland determined through visual identification. The baseline photocurrent measurement from the blank portion of the microscope slide was subtracted from each tissue fluorescence measurement. The resulting photocurrent due to autofluorescence was converted to incident radiant power, Φ_d, by using the detector responsivity at 550 nm (Table 1) as the nominal wavelength and with Eq. (2). The total fluorescence, Φ_s, was then estimated using Eq. (7), with the radiance emission, L_s, or radiant flux of total fluorescence emitted from the surfaces of illuminated tissue cross-section per unit solid angle, represented as a Lambertian source. In this study, more than 40 samples were evaluated.

2.3 Minocycline fluorescence verification

Minocycline, a naturally fluorescent antibiotic with excitation and emission centered at 390 nm and 500 nm, respectively, was tested in the form of a topical gel, an investigational drug product (BPX-01; at press time BPX-01 is a new drug product limited by United States law to investigational use only), on chosen tissue samples from low and high autofluorescence yield donors. A 2% BPX-01 prepared at 2.5 × (6.0 mg/cm^2), 8 × (20 mg/cm^2), and 25 × (60 mg/cm^2) daily doses, along with vehicle and untreated arms were topically applied to the surface of *ex vivo* human facial skin and incubated at 32 °C for 24 hours. The skin surface was cleaned of residual drug product and cryo-sectioned at 50 µm for investigation with conventional fluorescence microscopy (Fig. 1).

2.4 Fluorescence correlation: single- versus two-photon excitation

Sets of tissue samples spanning the radiance emission range were selected for spectral analysis by TPEF.

A modified confocal laser scanning microscope was used in this study (Olympus FV1000, Tokyo, Japan) equipped with a 20X objective lens (U Plan S-Apo, Olympus, Tokyo, Japan). Multiphoton excitation was provided by the output of a femtosecond optical parametric oscillator (OPO, Spectra-Physics DeepSee, Santa Clara, CA) introduced to the microscope side port. The OPO was tuned to 780 nm excitation wavelength, and set to expose samples to

Biomedical Optics EXPRESS

20-30 mW of average power. At the non-descanned epi port of the microscope, a 680 nm shortpass filter (680HQ-2P, Chroma Technologies, Bellows Falls, Vermont) was used to reject any remaining 780 nm excitation source.

Sample autofluorescence was reflected off a 750-nm longpass dichroic mirror into a multimode fiber bundle (Thorlabs BF20LSMA01, Newton, NJ) connected to a spectrometer (Ocean Optics QE 65000, Largo, FL). The TPEF spectra of 15 donor skin samples from three FOVs at three z-depths within the section (0, 15, and 20 μm) were measured by the spectrometer with a 10-second acquisition time while the laser continuously scanned the sample. One spectrum was generated from each FOV by averaging spectra from the three z-depths. For the quantification of autofluorescence signals, the spectral intensity from each FOV was integrated to find the area-under-the-curve. Subsequently, the average autofluorescence intensities of three FOVs from each donor were compared with results from fluorescence radiance emission characterization by the integrating sphere approach (Section 2.2.2.2)

3. Results

3.1 Human skin autofluorescence detection by integrating sphere and conventional fluorescence microscopy

To assess the endogenous autofluorescence present in facial skin, photons emitted from the tissue sample were collected by an integrating sphere and measured as a unit of photocurrent. 41 human facial skin specimens from 36 donors were evaluated by this method, and donor autofluorescence values (photocurrent) could be quantitatively differentiated. Autofluorescence ranging from 0.37 nA – 2.26 nA was recorded, corresponding to estimates of 14 μW – 81 μW in total fluorescence (Eqs. (2) and (7)) from the UV illuminated volume of the tissue cross-section. The average 386-nm UV excitation delivered through the 40 × objective lens to illuminate the 500-μm diameter FOV was approximately 21.2 mW. As only a finite cross-section of the tissue samples was illuminated with UV excitation, the total fluorescence may be represented with a meaningful parameter describing the amount of endogenous fluorescence produced per unit area per steradian – radiance emission, L_s. In this study, the corresponding radiance emission ranged from 1.09 mW/cm^2.sr to 6.57 mW/cm^2.sr, as shown in Fig. 5, equating to approximately a six-fold difference in tissue autofluorescence within the cohort tested.

Biomedical Optics EXPRESS

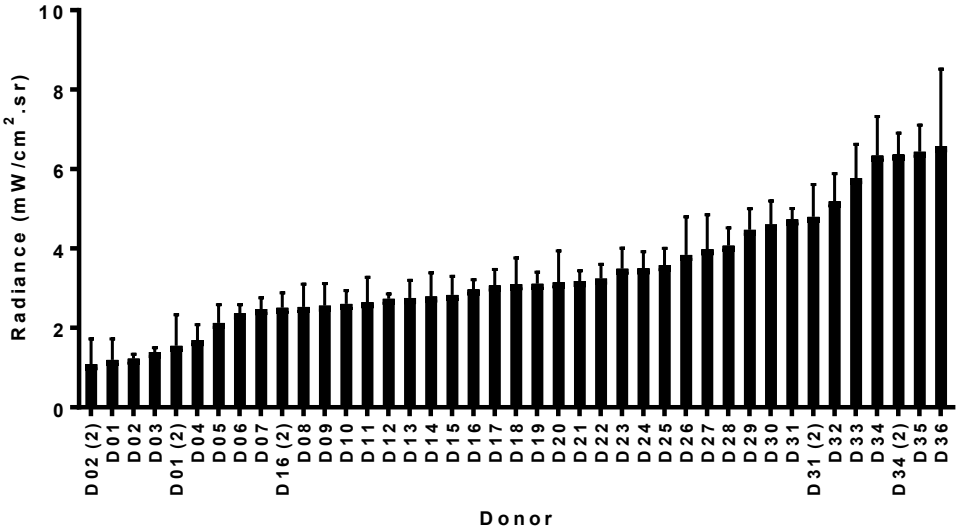

Fig. 5. Fluorescence radiance emission ranges 1.09 mW/cm^2.sr to 6.57mW/cm^2.sr was measured among specimens from different donors (sample size n = 41 donor n = 36). These quantitative results allow for direct comparison to the qualitative fluorescence intensity among the co-registered images captured during the experiment in Figs. 8, 9, and 10 below.

The fluorescence measurement results from 41 samples were assigned to groups of 1-mW/cm^2.sr radiance emission increment, and the population distribution was plotted as shown in Fig. 6(a). The mean radiance emission appeared to be approximately 3.38 mW/cm^2.sr though the population spread deviated from a normal distribution. There is a slightly steeper decline in the donor population toward low autofluorescence, while a more gradual decline in the donor population toward high autofluorescence from the mean value. This is also represented in a box-and-whisker plot shown in Fig. 6(b). The median radiance emission was 3.10 mW/cm^2.sr with 50% of the donors within the range of 2.52 – 4.27 mW/cm^2.sr fluorescence yield. Four donors exhibited values outside of the normal distribution's 95% confidence interval.

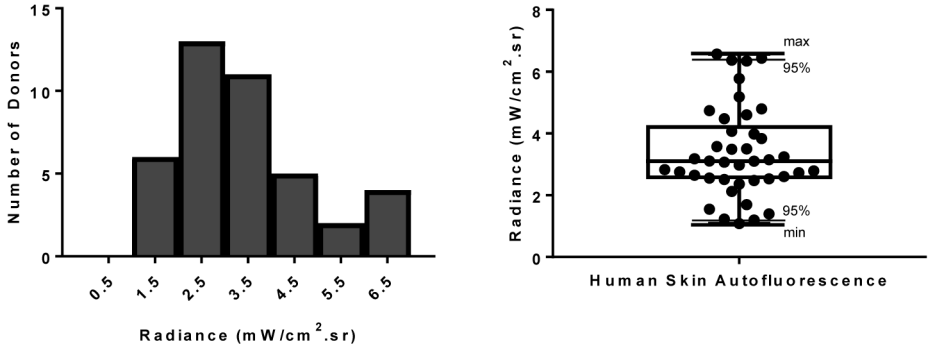

(a) (b)

Fig. 6. Additional analyses (a) indicate that when grouped into ranges of fluorescence radiance emission (n = 41 samples), the mean autofluorescence in the population was approximately 3.38 mW/cm^2.sr, with the population spread deviating from a normal distribution. (b) represent further distribution in a box-and-whisker plot where the population median was 3.10 mW/cm^2.sr. Four measurements exist outside the 95% confidence interval.

Biomedical Optics EXPRESS

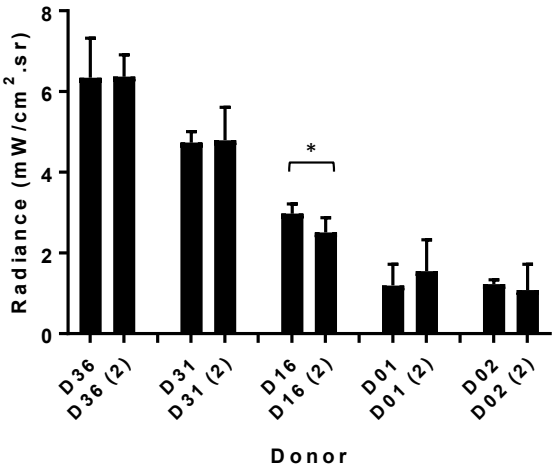

Fig. 7. Confirmation that sections with at least 150-μm intervals from previous measured section of the same donor show consistent measurements. *$P \leq 0.05$ by Student's T-test.

In addition, adjacent tissue sections at least 150 μm from the previous section were evaluated for tissue consistency within the same donor. As shown in Fig. 7, sections did not exhibit significant difference in fluorescence emission except for a single donor (D16).

Concurrent conventional wide-field fluorescence microscopy images were captured along with the total fluorescence measurements. Figures 8, 9 and 10 show qualitative increase in autofluorescence intensity from various donors, with direct correlation with the quantitative fluorescence radiance emission results from Fig. 5. Certain skin characteristics such as the pilosebaceous unit, may be of interest when observing topical drug delivery. In general, the majority of the FOV was occupied by these features. The fluorescence radiance emission across each figure ranged from low to high values among all donors sampled (D01 – D36). The FOV of tissue areas that included hair follicles are shown in Fig. 8 corresponding to a quantitative fluorescence range of 1.20 – 6.35 mW/cm^2.sr. Tissue areas including sebaceous glands are shown in Fig. 9 corresponding to a quantitative fluorescence range of 1.20 – 6.57 mW/cm^2.sr. Areas with both a hair follicle and sebaceous gland were also measured across the range of 1.20 – 6.35 mW/cm^2.sr, as shown in Fig. 10.

Qualitatively, a majority of the autofluorescence appeared to be in the 450-480 nm blue spectral region mostly originating from the dermal matrix, while it has been noted the epidermis and hair shaft could occasionally appear red (610-680 nm), as shown in Figs. 10(a)-10(c), or pinkish indicating a combination of fluorophores or broad-spectrum fluorescence (Fig. 8(e), epidermis). Most of the unoccupied areas in the follicle appeared dark (Fig. 8), and interestingly the sebaceous glands did not appear to emit within the passband of the emission filters (Fig. 9). It is worth noting that the contrast of the images was significant from the lowest to highest autofluorescing donors (Fig. 8(a)–8(i); Fig. 9(a)–9(i); Fig. 10(a)–10(d)), where the images appeared dim among the tissue samples with the lowest autofluorescence, but exhibited fluorescence emission that was close to detector saturation with the highest fluorescing samples.

Biomedical Optics EXPRESS

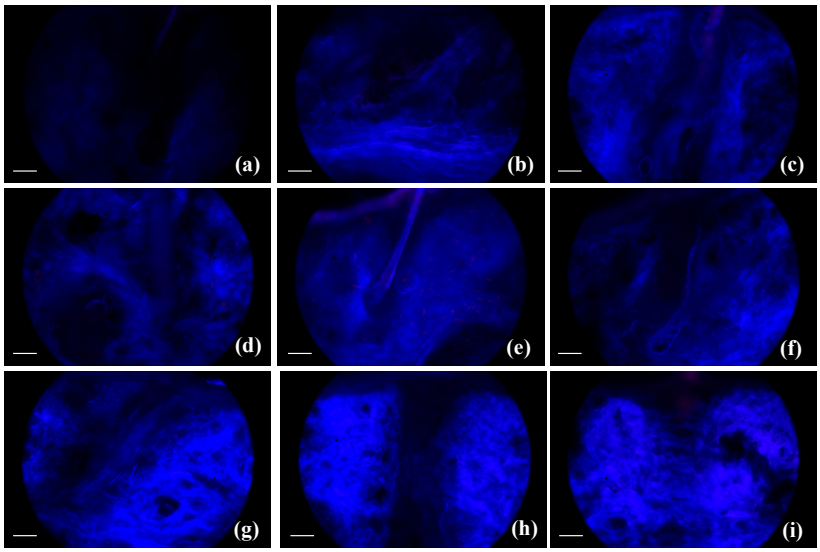

Fig. 8. Images of hair follicles from various donors exhibiting increasing autofluorescence (a) D01; 1.20 mW/cm^2.sr, (b) D04; 1.69 mW/cm^2.sr, (c) D12; 2.73 mW/cm^2.sr, (d) D20; 3.15 mW/cm^2.sr, (e) D25; 3.58 mW/cm^2.sr, (f) D28; 4.07 mW/cm^2.sr, (g) D31; 4.73 mW/cm^2.sr, (h) D33; 5.78 mW/cm^2.sr, and (i) D34; 6.35 mW/cm^2.sr. Qualitative increase in fluorescence in these images are in correlation to quantitative measurements of fluorescence in Fig. 5. Autofluorescence from the blue spectrum appeared to dominate, with slight red-channel fluorescence in the epidermis (e). Fluorescence was measured and images captured with fluorescence originating from within the 500-µm circular FOV using a 40 × objective lens. Scale bar represents 50 µm.

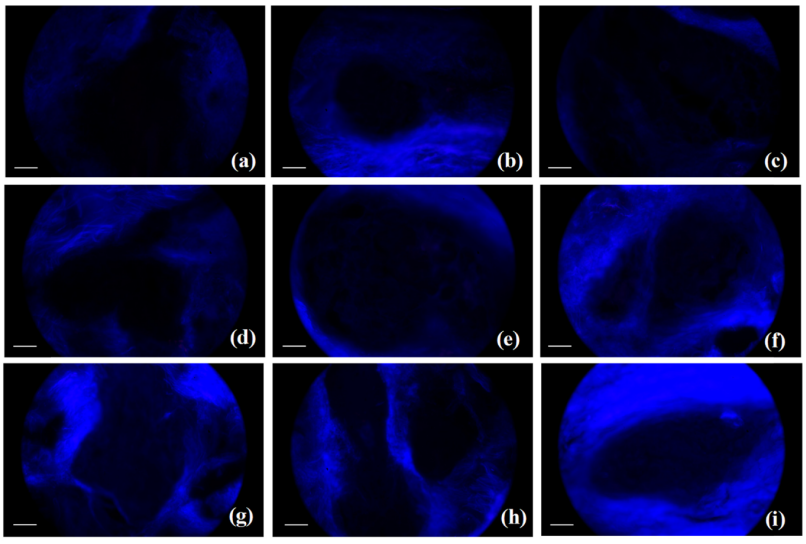

3

Fig. 9. Images of sebaceous glands from various donors exhibiting increasing autofluorescence (a) D01; 1.20 mW/cm^2.sr, (b) D04; 1.69 mW/cm^2.sr, (c) D10; 2.60 mW/cm^2.sr, (d) D18; 3.10 mW/cm^2.sr, (e) D25; 3.58 mW/cm^2.sr, (f) D28; 4.07 mW/cm^2.sr, (g) D30; 4.60 mW/cm^2.sr, (h) D33; 5.78 mW/cm^2.sr, and (i) D36; 6.57 mW/cm^2.sr. Qualitative increase in fluorescence in these images are in correlation to quantitative measurements of fluorescence in Fig. 5. Autofluorescence from the blue spectrum appeared to dominate, with no observable red fluorescence under the experimental conditions. Fluorescence was measured and images captured with fluorescence originating from within the 500-µm circular FOV using a 40 × objective lens. Scale bar represents 50 µm.

Biomedical Optics EXPRESS

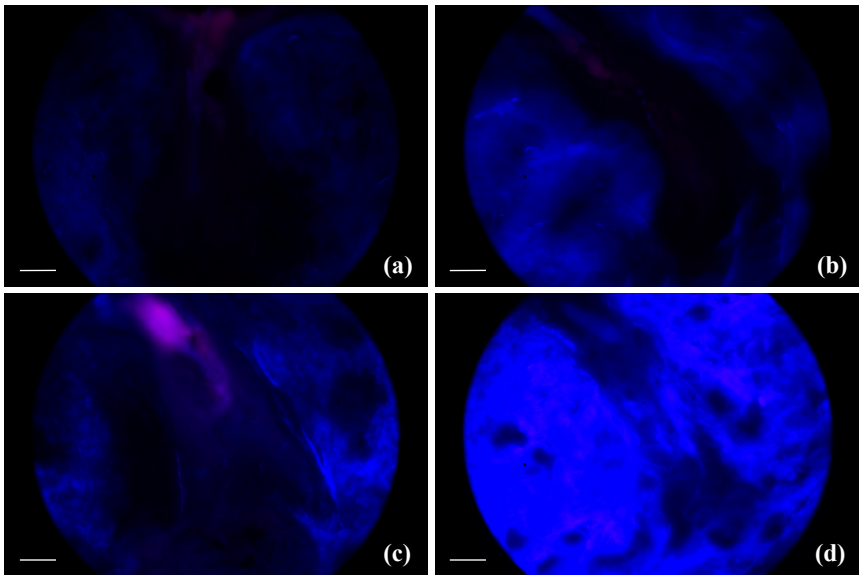

Fig. 10. Images consisting of hair follicle with adjacent sebaceous glands from various donors exhibiting increasing autofluorescence (a) D01; 1.20 mW/cm^2.sr, (b) D17; 3.07 mW/cm^2.sr, (c) D31; 4.73 mW/cm^2.sr, and (d) D34; 6.35 mW/cm^2.sr. Qualitative increase in fluorescence in these images are in correlation to quantitative measurements of fluorescence in Fig. 5. Autofluorescence from the blue spectrum appeared to dominate, with red-channel fluorescence detected in the hair follicles (a,b,c). Fluorescence was measured and images captured with fluorescence originating from within the 500-µm circular FOV using a 40 × objective lens. Scale bar represents 50 µm.

3.2 Verification: conventional fluorescence microscopy with minocycline

Figure 11 portrays the outcome of conventional fluorescence microscopy of minocycline delivery in a topical gel on *ex vivo* human facial skin specimens having low autofluorescence (Fig. 11(a), D06) and high autofluorescence (Fig. 11(b), D32). Comparing the untreated and vehicle controls of the two donor tissues, it was obvious that the high autofluorescence donor (D32) exhibited higher endogenous fluorescence, specifically in the dermis as shown in the composite images consisting of significant amount of autofluorescence in the 450-480 nm (blue) region. When the RBG images from our digital camera were separated into red and blue channels, the untreated and vehicle treated groups for low-autofluorescence donor D06 were found to have no detectable autofluorescence under the experimental conditions (Fig. 11(a), untreated and vehicle). In contrast, the red color channel for untreated and vehicle images acquired from the high-autofluorescence donor D32 showed red autofluorescence arising from the dermal matrix and sebaceous glands. As the skin autofluorescence spectrum is known to have a rather long red emission tail [14], the red-channel autofluorescence difference between the low and high autofluorescence is thought to arise due to the higher total tissue autofluorescence levels of donor D32 that contributed to the detectable red channel fluorescence emission.

In all treated tissues of donor D32, the raw/composite images appeared to only show minocycline signal at the superficial layers, but when the images were separated into blue and red channels, red fluorescence emission from the deeper mid- and reticular dermis was revealed. By comparison, treated tissues of both D06 and D32 exhibited incremental minocycline fluorescence intensities from 2.5 × , 8 × , to 25 × daily doses, as expected. It should be noted, however, that the red spectral emission detected in the high autofluorescence donor complicates a straightforward quantification of minocycline, as both emit within the same wavelength range. Selecting donors observed to have low total autofluorescence levels

Biomedical Optics EXPRESS

would remove this complication and enable more robust drug fluorescence emission quantification.

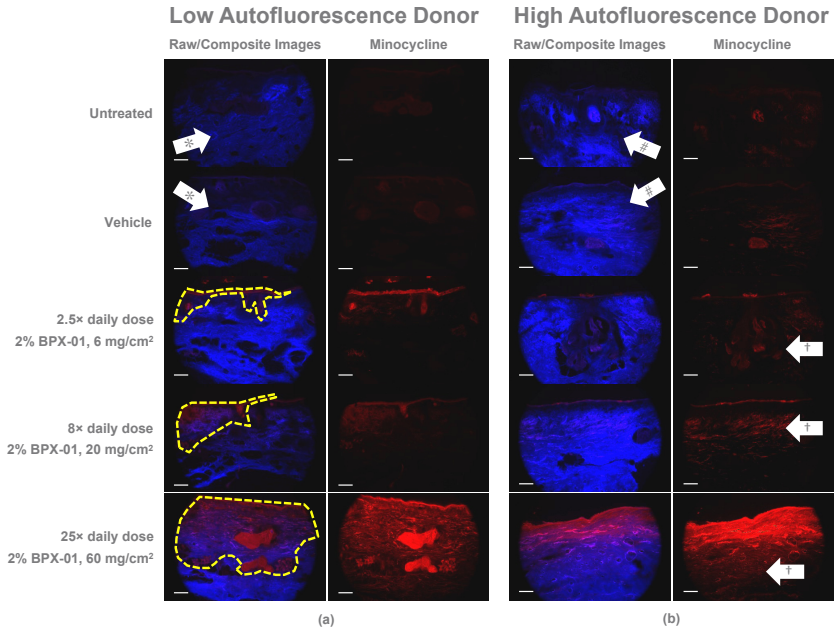

Fig. 11. Conventional fluorescence microscopy images of tissues from (a) low autofluorescence donor, D06, and (b) high autofluorescence donor, D32, in an *ex vivo* penetration study of 2.5 × , 8 × , and 25 × daily doses of a 2% topical minocycline gel along with vehicle and untreated controls. * arrows indicate mainly low (blue) autofluorescence of D06, while # arrows indicate mainly high autofluorescence of D32. Left columns in (a) and (b) are raw images, and right columns are segmentation of mainly (red) minocycline fluorescence from 610 to 680 nm. Note that no red fluorescence was detectable in the untreated and vehicle arms of D06, while slight red autofluorescence was noticeable in D32. Yellow dotted line areas in the treated D06 donor tissues indicated perceptible minocycline fluorescence matching the corresponding segmented images to the right. However, in the treated D32 donor tissues, the delivery into the deeper dermal layer, indicated by † arrows, was only perceptible after segmentation of the 610-680 nm signals. 10x objective, scale bar represents 200 µm. Both image sets were captured with the same acquisition parameters.

3.3 Correlation: fluorescence correlation of UV-excited conventional fluorescence microscopy versus two-photon excitation fluorescence microscopy

To ultimately follow minocycline uptake in living skin to capture pharmacokinetics, TPEF microscopy offers considerable advantages over conventional fluorescence imaging. To see if autofluorescence data measured by this integrating sphere approach could be carried over to multiphoton investigations, the samples were analyzed by TPEF. Figure 12 compares the two-photon excited fluorescence intensity with the UV-excited fluorescence radiance emission measurements (Figs. 1 and 5) from 15 donors. Although the background tissue autofluorescence levels measured by TPEF and integrating sphere characterizations did not trend exactly amongst the 15 pairs of donors, an overall fair correlation between the two data sets was obtained (Pearson's correlation coefficient, $r = 0.613$, $p = 0.015$, Fig. 12).

Biomedical Optics EXPRESS

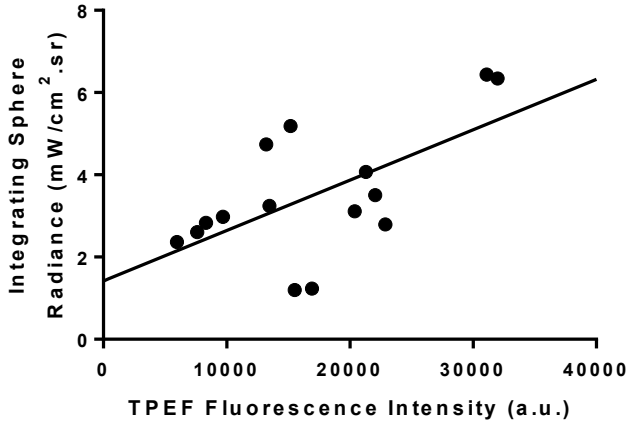

Fig. 12. Autofluorescence spectral intensity of 15 donor tissue specimens with TPEF/spectrometer and conventional fluorescence microscopy/integrating sphere measurements. Results from the two data sets were compared using Pearson's correlation. The analysis indicted fair relative agreement of single- and two-photon excited fluorescence yield (Pearson's correlation coefficient, $r = 0.613$, $p = 0.015$).

4. Discussion

Due to varying morphology and heterogeneity in the distribution of endogenous fluorophores in the skin, conducting topical drug delivery studies with donor tissues may produce unpredictable levels of SNR and limit the detectability of fluorescence originating from the active pharmaceutical ingredient (API) of interest.

An integrating sphere was combined with a conventional fluorescence microscope to quantify the endogenous fluorescence profile of *ex vivo* human facial skin specimens. This setup was used with the intent of developing a fluorescence microscopy screening tool for studies involving the identification and distribution of exogenous fluorophores such as minocycline. In this integrating sphere approach, the tissue specimen was placed as close as possible to the input aperture of the integrating sphere, such that autofluorescence collection could be carried out simultaneously with image capture of the same FOV. This method also avoided interface/Fresnel loss from relaying imaging optics as well as concerns of collecting stray light originating beyond the acceptance angle of the imaging system. The latter could occur when fluorescence outside of the acceptance angle bounces off internal walls of the optomechanical construct holding the lens assembly and re-enters the imaging system within the acceptance angle. The integrating sphere also 'scrambled' any chromatic dispersion of the endogenous fluorescence spectra representing various constituent fluorophores within the tissue, ensuring a uniform distribution of component spectra at the photodetector. Finally, this technique minimizes any non-uniform spatial and angular incidence of fluorescence directly on a photodetector that could add inconsistency to the measurement.

Within the cohort of donor tissues in this study, a significant distinction among donor endogenous fluorescence was observed, with approximately six-fold differential measured (Fig. 5). The estimated fluorescence radiance emission ranged from 1.09 – 6.57 mW/cm^2.sr with a mean at 3.38 mW/cm^2.sr (Fig. 6(a)) and a median at 3.10 mW/cm^2.sr (Fig. 6(b)). These samples were processed at room temperature (25 °C) after which sections were allowed to dry on microscope slides. However, temperature or hydration of the tissue may affect fluorescence yield and warrant further exploration [27,28]. The fluorescent intensities from the epidermis, hair follicles and sebaceous glands captured in images acquired with conventional microscopy tracked the yield trend of endogenous fluorescence from individual donors and provided qualitative comparatives to the measurements (Figs. 5, 8–10).

Biomedical Optics EXPRESS

Measurements provided representative endogenous fluorescence levels from the donors, as demonstrated in Fig. 7, where sections from different skin areas from the same donor exhibited consistent results. To our knowledge, this is the first study conducted to assess the differences and range in endogenous fluorescence of a large cohort of human facial skin specimens.

Previous studies of quantitative autofluorescence measurements have focused on spectroscopy, relative fluorescence, and fluorescence spectra of endogenous species [29,30]. While it is straightforward to measure extrinsic fluorescence [31], numerous approaches to measuring or estimating the intrinsic fluorescence arising from turbid media have been attempted. These approaches involved approximation using diffusion theory, Monte Carlo model, empirical methods such as subtraction and ratio techniques, and other variations each having its own limitations [32,33]. In general, the difficulty in extracting intrinsic fluorescence arises because absorption and scattering from the tissue distort the fluorescence spectra of the fluorophores. Zhang *et al.* estimated differences in skin fluorescence of healthy versus diabetic subjects with the latter exhibiting higher extrinsic and intrinsic fluorescence. Interestingly, extrinsic fluorescence measurements suggested an approximate 4-fold difference should exist at the spectral peak (~510 nm), while only about 2-fold difference in recovered intrinsic fluorescence was observed at the tissue spectral peak (~480 nm). Gamm *et al*. demonstrated intrinsic fluorescence yield approximation of fluorescein in turbid media in the range of 0.05%-0.07% at the spectral peak, with varying degree of absorbers having optical properties similar to that of tissue [32]. Our experimental approach involved tissue sections that were relatively thick by comparison to the effective optical penetration depth of skin at 386 nm in the UV, which is dominated by Rayleigh scattering. On the other hand, the tissues were thinner than the effective optical penetration depths of the fluorescence in the visible and near infrared spectrum [34]. As a result, a significant fraction of the UV excitation light was attenuated within the tissue section, while the fluorescence emission should have undergone minimal distortion through local re-absorption and scattering. The measured fluorescence conversion efficiency of our data set, which is the ratio of fluorescence emission integrated from 450 to 680 nm over the excitation power, provided a range of 0.06% – 0.39% from low to high autofluorescence donors, with the limitation that the diffuse reflectance was unknown. This range is interestingly within an order of magnitude difference from intrinsic fluorescence estimated by Gamm *et al.* at the spectral peak (not spectrally integrated values) in their tissue phantoms. In our case, further work to account for the effects of tissue optical properties, diffuse reflectance and transmission loss is warranted.

Endogenous fluorescence arises from various constituents in human skin such as NAD(P)H, porphyrins, collagen, elastin and keratin, making it difficult to differentiate exogenous fluorophores such as active pharmaceutical ingredients (API) from those of skin background. For instance, spectral overlap exists between minocycline and collagen (λ_{ex} ~335/370 nm), keratin (λ_{ex} ~370 nm), and NAD(P)H (λ_{ex} ~350 nm) in the 460 nm emission range and porphyrins (λ_{ex} ~405) in the 620 nm emission range [14,29]. Both porphyrins and NADH may be present in the sebaceous glands where minocycline is expected to accumulate. Imaging results from untreated skin in this study produced occasional observable 620 nm range fluorescence in the hair follicle and sebaceous gland, indicative of porphyrin/NADH (Fig. 10(a)-10(c)) especially those with high autofluorescence (Fig. 11(b), untreated and vehicle). Elevated levels of endogenous fluorescence have been attributed to age, gender, lifestyle, Fitzpatrick skin types, genetics, etc [12–21]. Independent findings by Leffell et al., Takema et al., Stamatas et al., and Sandby-Møller et al. [35–38] have suggested that the leading cause of changes in cutaneous autofluorescence level could be chronic UV exposure and photoaging. It is worth noting that, from the donors evaluated at ages 42–78 years old in this study, no correlation was observed between the endogenous fluorescence and donor age and there was no known lifestyle information to elicit the role of sun exposure. However, elevated endogenous fluorescence in the red spectrum, such as those of porphyrin and

Biomedical Optics EXPRESS

NADH, could confound the measurements of exogenous fluorescence from minocycline in our case. A previous study had indicated that the autofluorescence profile may differ between fresh and frozen skin samples, due to loss of fluorescing metabolic by-products in freshly excised skin, which warrants further investigation [39].

When minocycline in the form of a topical gel (2% BPX-01) penetrated the skin, the low autofluorescence donors exhibited more apparent minocycline signal in the dermis of the original composite images in comparison to the high autofluorescence donor (Fig. 11). The segmented red channel appeared to provide for more reliable images of minocycline distribution, while the composite images tended to mask minocycline fluorescence of its contribution in donor tissues of high autofluorescence.

The autofluorescence screening results largely hold under two-photon excitation with a moderately strong correlation observed between the one- and two-photon results. This indicates that the results from the integrating sphere method are applicable to more advanced microscopy methods. As shown in Fig. 12, autofluorescence of tissues from 15 donors (sequential sections) were compared. Because TPEF microscopy has an intrinsic sectioning due to the nonlinear excitation process, the effective sampling depth (and hence volume) is much smaller than under wide field fluorescence imaging. We suggest that the moderately strong correlation with TPEF (Pearson's correlation coefficient, $r = 0.613$, $p = 0.015$, Fig. 12) is a natural outcome in the difference between wide-field and two-photon experimental setups. Supporting this explanation is the observation that a high variance of autofluorescence spectral signals between FOVs within the same tissue was observed under two-photon excitation. This would be expected if the two-photon method sparsely samples the skin's inherently heterogenous compositions, whereas the integrating sphere approach accumulates autofluorescence throughout the volume cross-section of the 50-μm tissue within the FOV. It is also worth noting that the two-photon and one-photon excitation spectra are not always similar, which could also lead to differences between the emission quantified by the two methods. A future study to elucidate the utility of tissue autofluorescence screening to TPEF microscopy of minocycline or other API-dosed tissues is warranted.

In this study, the integrating sphere approach created a space constraint requiring the tissue sample and the microscope slide to be sandwiched between the integrating sphere and the objective lens. Improvements can be made by automating the xyz stage motion control and collecting the data directly with control software and a user interface via a computer, enabling less work-intensive experimentation and more consistent, accurate results. Also, the microscope UV excitation lightsource being a mercury arc lamp, continuously degrades overtime while in use potentially causing output power fluctuation, unlike Xenon arc sources which are typically more stable. In our case, the mercury arc lamp was stabilized by allowing it to warm up for a short period prior to experimentation. In future studies, a consistent lightsource such as LED would improve reliability and repeatability of our experiment over a long sampling period (days). To temporarily mitigate this concern, the output power of the microscope lightsource delivered through the objective lens was monitored for 7 days with Intralipid-10% as the reference standard [24,40], well within the period during which the data presented in this article was collected. Further, baseline power measurements were monitored during each experiment session and baseline photocurrents were recorded for each tissue section.

The use of fluorescence microscopy in the study of drug pharmacokinetics is a relatively new development [7,11]. While this study explored the utility of single-photon excited fluorescence microscopy in *ex vivo* drug delivery, this and other nonlinear microscopy techniques are translationally viable options for *in vivo* cutaneous pharmacokinetic tomography. The immediate benefit of optical microscopy is visualization of drug delivery and distribution in high resolution, which in this case could be a few microns or less. For future improvements, confocal and nonlinear microscopy could be pushed to the diffraction-limit, providing spatial specificity that no existing autoradiography and MSI techniques could

Biomedical Optics EXPRESS

achieve [41–43]. To date, the use of nonlinear optical imaging modalities such as multiphoton excitation [44], FLIM [45], Stimulated Raman Scattering [46], and Coherent Anti-Stokes Raman Scattering [47,48] microscopies have focused on high resolution functional and structural imaging. These tools have enabled visualization of cellular and subcellular metabolism, granules, tumorous lesions, and differentiation of functional proteins. Moreover, these nonlinear imaging tools may also provide more specificity to the exogenous molecules being identified.

In dermatology, in particular, there is a need to understand the delivery and diffusion of drugs of topically-administered products through the skin barrier (e.g. stratum corneum) and hair follicle. This information is critical in early stage drug development in screening API and determining the optimal dosages or concentrations. The spatiotemporal distribution of an API may provide insight into understanding its safety and efficacy before clinical studies are initiated. The impact of this information is significant in terms of technical and financial implications. For instance, the accumulation of API in the stratum corneum with slow diffusion rate into the epidermis or dermis may indicate poor solubility and bioavailability as well as a cause of unacceptable drug-related irritation or side effects. Even if the API is known to be effective when properly delivered to its target tissues, poor bioavailability and a high risk of cutaneous irritation may be the reasons to abandon further clinical development.

5. Conclusion

In this study, we presented the use of an integrating sphere coupled to a fluorescence microscope to measure human facial skin endogenous fluorescence and capture fluorescence images concurrently. We measured a fluorescence radiance emission range of 1.09 – 6.57 $mW/cm^2.sr$, a six-fold difference, from human facial skin specimens among a group of more than 35 donors. This is the first quantitative assessment undertaken, to the best of our knowledge, to shed light on the significant differences in endogenous skin fluorescence among a large group of individuals. In addition to single-photon excited autofluorescence, these measurements were compared to two-photon excited autofluorescence spectral intensity which exhibited a fair correlation between the two data sets. The results indicate that a high autofluorescence level of tissue could also interfere in the visualization of fluorescent drug even under two-photon excitation condition. This suggests that pre-screening subjects for low autofluorescence in translational research may aid in visualizing and potentially quantifying exogenous fluorophores, such as that of a drug, at the very least with single-photon excited fluorescence microscopy to elucidate drug delivery and distribution within the skin when the drug distribution profile overlaps with the endogenous fluorophores.

Acknowledgments

This study was funded via a sponsored research agreement between Massachusetts General Hospital and BioPharmX, Inc.

Disclosures

The authors declare no competing financial interests.

References

1. D. Zhang and S. Surapaneni, *ADME-Enabling Technologies in Drug Design and Development* (John Wiley & Sons, Inc. 2012).
2. E. G. Solon, "Autoradiography techniques and quantification of drug distribution," Cell Tissue Res. **360**(1), 87–107 (2015).
3. E. G. Solon, A. Schweitzer, M. Stoeckli, and B. Prideaux, "Autoradiography, MALDI-MS, and SIMS-MS Imaging in Pharmaceutical Discovery and Development," AAPS J. **12**(1), 11–26 (2010).
4. V. Raufast and A. Mavon, "Transfollicular delivery of linoleic acid in human scalp skin: permeation study and microautoradiographic analysis," Int. J. Cosmet. Sci. **28**(2), 117–123 (2006).
5. C. Cardoso-Palacios and I. Lanekoff, "Direct Analysis of Pharmaceutical Drugs Using Nano-DESI MS," J. Anal. Methods Chem. **2016**, 3591908 (2016).

Biomedical Optics EXPRESS

6. J. Ling, S. D. Weitman, M. A. Miller, R. V. Moore, and A. C. Bovik, "Direct Raman imaging techniques for study of the subcellular distribution of a drug," Appl. Opt. **41**(28), 6006–6017 (2002).
7. C. A. Thorling, Y. Dancik, C. W. Hupple, G. Medley, X. Liu, A. V. Zvyagin, T. A. Robertson, F. J. Burczynski, and M. S. Roberts, "Multiphoton microscopy and fluorescence lifetime imaging provide a novel method in studying drug distribution and metabolism in the rat liver in vivo," J. Biomed. Opt. **16**(8), 086013 (2011).
8. S. F. El-Mashtoly, D. Petersen, H. K. Yosef, A. Mosig, A. Reinacher-Schick, C. Kötting, and K. Gerwert, "Label-free imaging of drug distribution and metabolism in colon cancer cells by Raman microscopy," Analyst (Lond.) **139**(5), 1155–1161 (2014).
9. T. Losanno and C. Gridelli, "Recent advances in targeted advanced lung cancer therapy in the elderly," Expert Rev. Anticancer Ther. **17**(9), 787–797 (2017).
10. G. S. Herron, D. Lac, M. Hermsmeier, X. Chen, S. Y. Huang, N. Yam, A. Yamamoto, U. Nagavarapu, and K. F. Chan, "BPX-01: A Novel Hydrophilic Formulation for Treatment of Acne Vulgaris," SDEF 11th Annual Women's and Pediatric Dermatology Seminar, Newport Beach, October 23–24, 2015.
11. S. Jeong, M. Hermsmeier, S. Osseiran, A. Yamamoto, U. Nagavarapu, K. F. Chan, and C. L. Evans, "Visualization of drug distribution of a topical minocycline gel in human facial skin," Biomed. Opt. Express **9**(7), 3434–3448 (2018).
12. R. P. van Waateringe, S. N. Slagter, M. M. van der Klauw, J. V. van Vliet-Ostaptchouk, R. Graaff, A. D. Paterson, H. L. Lutgers, and B. H. R. Wolffenbuttel, "Lifestyle and clinical determinants of skin autofluorescence in a population-based cohort study," Eur. J. Clin. Invest. **46**(5), 481–490 (2016).
13. M. S. Ahmad, Z. A. Damanhouri, T. Kimhofer, H. H. Mosli, E. Holmes, "A new gender-specific model for skin autofluorescence risk stratification," Sci. Rep. **5**, 10198 (2015).
14. K. König, H. Meyer, H. Schneckenburger, and A. Rück, "The Study of Endogenous Porphyrins in Human Skin and Their Potential for Photodynamic Therapy by Laser Induced Fluorescence Spectroscopy," Lasers Med. Sci. **8**(2), 127–132 (1993).
15. A. Nongnuch and A. Davenport, "The effect of vegetarian diet on skin autofluorescence measurements in haemodialysis patients," Br. J. Nutr. **113**(7), 1040–1043 (2015).
16. R. Bazin, F. Flament, A. Colonna, R. Le Harzic, R. Bückle, B. Piot, F. Laizé, M. Kaatz, K. König, and J. W. Fluhr, "Clinical study on the effects of a cosmetic product on dermal extracellular matrix components using a high-resolution multiphoton tomograph," Skin Res. Technol. **16**(3), 305–310 (2010).
17. L. McDonald, B. Liu, A. Taraboletti, K. Whiddon, L. P. Shriver, M. Konopka, Q. Liu, and Y. Pang, "Fluorescent flavonoids for endoplasmic reticulum cell imaging," J. Mater. Chem. B Mater. Biol. Med. **4**(48), 7902–7908 (2016).
18. D. C. Bos, W. L. de Ranitz-Greven, and H. W. de Valk, "Advanced glycation end products, measured as skin autofluorescence and diabetes complications: a systematic review," Diabetes Technol. Ther. **13**(7), 773–779 (2011).
19. C. C. Wang, Y. C. Wang, G. J. Wang, M. Y. Shen, Y. L. Chang, S. Y. Liou, H. C. Chen, A. S. Lee, K. C. Chang, W. Y. Chen, and C. T. Chang, "Skin autofluorescence is associated with inappropriate left ventricular mass and diastolic dysfunction in subjects at risk for cardiovascular disease," Cardiovasc. Diabetol. **16**(1), 15 (2017).
20. F. E. van Dooren, F. Pouwer, C. G. Schalkwijk, S. J. Sep, C. D. Stehouwer, R. M. Henry, P. C. Dagnelie, N. C. Schaper, C. J. van der Kallen, A. Koster, J. Denollet, F. R. Verhey, and M. T. Schram, "Advanced Glycation End Product (AGE) Accumulation in the Skin is Associated with Depression: The Maastricht Study," Depress. Anxiety **34**(1), 59–67 (2017).
21. R. P. van Waateringe, S. N. Slagter, A. P. van Beek, M. M. van der Klauw, J. V. van Vliet-Ostaptchouk, R. Graaff, A. D. Paterson, H. L. Lutgers and B. H. R. Wolffenbuttel, "Skin autofluorescence, a non-invasive biomarker for advanced glycation end products, is associated with the metabolic syndrome and its individual components," Diabetol. Metab. Syndr. **9**, 42 (2017).
22. S. Schneider, M. O. Schmitt, G. Brehm, M. Reiher, P. Matousek, and M. Towrie, "Fluorescence kinetics of aqueous solutions of tetracycline and its complexes with Mg^{2+} and Ca^{2+}," Photochem. Photobiol. Sci. **2**(11), 1107–1117 (2003).
23. J. Guyotat, J. Pallud, X. Armoiry, V. Pavlov, and P. Metellus, "5-Aminolevulinic Acid-Protoporphyrin IX Fluorescence-Guided Surgery of High-Grade Gliomas: A Systematic Review," Adv. Tech. Stand. Neurosurg. **43**, 61–90 (2016).
24. H. J. van Staveren, C. J. M. Moes, J. van Marie, S. A. Prahl, and M. J. C. van Gemert, "Light scattering in Intralipid-10% in the wavelength range of 400-1100 nm," Appl. Opt. **30**(31), 4507–4514 (1991).
25. Integrating Sphere Theory and Applications, Technical Guide, Labsphere a Halma Company.
26. B. G. Grant, *Field Guide to Radiometry* (SPIE Press, 2011).
27. R. T. Zaman, N. Rajaram, A. Walsh, J. Oliver, H. G. Rylander 3rd, J. W. Tunnell, A. J. Welch, and A. Mahadevan-Jansen, "Variation of fluorescence in tissue with temperature," Lasers Surg. Med. **43**(1), 36–42 (2011).
28. A. J. Walsh, D. B. Masters, E. D. Jansen, A. J. Welch, and A. Mahadevan-Jansen, "The effect of temperature on the autofluorescence of scattering and non-scattering tissue," Lasers Surg. Med. **44**(9), 712–718 (2012).
29. N. Kollias, G. Zonios, and G. N. Stamatas, "Fluorescence spectroscopy of skin," Vib. Spectrosc. **28**(1), 17–23 (2002).

Biomedical Optics EXPRESS

30. L. H. Laiho, S. Pelet, T. M. Hancewicz, P. D. Kaplan, and P. T. C. So, "Two-photon 3-D mapping of ex vivo human skin endogenous fluorescence species based on fluorescence emission spectra," J. Biomed. Opt. **10**(2), 024016 (2005).
31. V. N. Du Le, Z. Nie, J. E. Hayward, T. J. Farrell, and Q. Fang, "Measurements of extrinsic fluorescence in Intralipid and polystyrene microspheres," Biomed. Opt. Express **5**(8), 2726–2735 (2014).
32. U. A. Gamm, C. L. Hoy, F. van Leeuwen-van Zaane, H. J. Sterenborg, S. C. Kanick, D. J. Robinson, and A. Amelink, "Extraction of intrinsic fluorescence from single fiber fluorescence measurements on a turbid medium: experimental validation," Biomed. Opt. Express **5**(6), 1913–1925 (2014).
33. Y. Zhang, H. Hou, Y. Zhang, Y. Wang, L. Zhu, M. Dong, and Y. Liu, "Tissue intrinsic fluorescence recovering by an empirical approach based on the PSO algorithm and its application in type 2 diabetes screening," Biomed. Opt. Express **9**(4), 1795–1808 (2018).
34. A. N. Bashkatov, E. A. Genina, V. I. Kochubey, and V. V. Tuchin, "Optical properties of human skin, subcutaneous and mucous tissues in the wavelength range from 400 to 2000 nm," J. Phys. D Appl. Phys. **38**(15), 2543–2555 (2005).
35. D. J. Leffell, M. L. Stetz, L. M. Milstone, and L. I. Deckelbaum, "*In vivo* fluorescence of human skin. A potential marker of photoaging," Arch. Dermatol. **124**(10), 1514–1518 (1988).
36. Y. Takema, Y. Yorimoto, H. Ohsu, O. Osanai, and M. Kawai, "Age-related discontinuous changes in the in vivo fluorescence of human facial skin," J. Dermatol. Sci. **15**(1), 55–58 (1997).
37. G. N. Stamatas, R. B. Estanislao, M. Suero, Z. S. Rivera, J. Li, A. Khaiat, and N. Kollias, "Facial skin fluorescence as a marker of the skin's response to chronic environmental insults and its dependence on age," Br. J. Dermatol. **154**(1), 125–132 (2006).
38. J. Sandby-Møller, E. Thieden, P. A. Philipsen, J. Heydenreich, and H. C. Wulf, "Skin autofluorescence as a biological UVR dosimeter," Photodermatol. Photoimmunol. Photomed. **20**(1), 33–40 (2004).
39. W. Y. Sanchez, T. W. Prow, W. H. Sanchez, J. E. Grice, and M. S. Roberts, "Analysis of the metabolic deterioration of ex vivo skin from ischemic necrosis through the imaging of intracellular NAD(P)H by multiphoton tomography and fluorescence lifetime imaging microscopy," J. Biomed. Opt. **15**(4), 046008 (2010).
40. V. N. Du Le, Z. Nie, J. E. Hayward, T. J. Farrell, and Q. Fang, "Measurements of extrinsic fluorescence in Intralipid and polystyrene microspheres," Biomed. Opt. Express **5**(8), 2726–2735 (2014).
41. E. G. Solon and L. Kraus, "Quantitative whole-body autoradiography in the pharmaceutical industry. Survey results on study design, methods, and regulatory compliance," J. Pharmacol. Toxicol. Methods **46**(2), 73–81 (2001).
42. L. A. McDonnell, R. M. A. Heeren, R. P. J. de Lange, and I. W. Fletcher, "Higher sensitivity secondary ion mass spectrometry of biological molecules for high resolution, chemically specific imaging," J. Am. Soc. Mass Spectrom. **17**(9), 1195–1202 (2006).
43. M. Kubicek, G. Holzlechner, A. K. Opitz, S. Larisegger, H. Hutter, and J. Fleig, "A novel ToF-SIMS operation mode for sub 100 nm lateral resolution: application and performance," Appl. Surf. Sci. **289**(100), 407–416 (2014).
44. W. Denk, J. H. Strickler, and W. W. Webb, "Two-photon laser scanning fluorescence microscopy," Science **248**(4951), 73–76 (1990).
45. J. R. Lakowicz, H. Szmacinski, K. Nowaczyk, and M. L. Johnson, "Fluorescence lifetime imaging of free and protein-bound NADH," Proc. Natl. Acad. Sci. U.S.A. **89**(4), 1271–1275 (1992).
46. C. W. Freudiger, W. Min, B. G. Saar, S. Lu, G. R. Holtom, C. He, J. C. Tsai, J. X. Kang, and X. S. Xie, "Label-free biomedical imaging with high sensitivity by stimulated Raman scattering microscopy," Science **322**(5909), 1857–1861 (2008).
47. M. Muller, J. Squier, and G. J. Brakenhoff, "CARS microscopy with folded BoxCARS phasematching," J. Microsc. **197**(2), 150–158 (2000).
48. C. L. Evans, E. O. Potma, M. Puoris'haag, D. Côté, C. P. Lin, and X. S. Xie, "Chemical imaging of tissue in vivo with video-rate coherent anti-Stokes Raman scattering microscopy," Proc. Natl. Acad. Sci. U.S.A. **102**(46), 16807–16812 (2005).